Bionic Seal Whisker Triboelectric Sensor for Underwater Multiobject Wake Perception

Jianhua Liu, Siyuan Wang, Yuanzheng Li, Ziyue Xi, Hao Jin, Peng Xu, and Minyi Xu

***Abstract*—Existing underwater flow field sensing techniques encounter significant challenges in complex and variable flow environments. Seals possess a highly sensitive whisker sensing system that enables them to perform tasks such as predation and environment sensing. Drawing inspiration from the hydrodynamic tactile function of seal whiskers, this article introduces a bionic whisker triboelectric sensor (BWTS) that integrates whisker-based sensing mechanisms with triboelectric nanogenerator technology. The BWTS features a wavy bionic whisker and a flexible bionic follicle structure embedded with four sensing units. It is verified through simulation and experimental analysis that the BWTS can effectively capture the wake field characteristics of stationary and moving underwater objects under different flow field parameters. The BWTS demonstrates high reliability, achieving correlation coefficients of 0.98–0.99 for the geometrical and kinematic parameters of underwater objects. The error is less than 10%. Additionally, its strong directional recognition and flow field feature sensing capabilities have been validated. As a noncontact underwater flow field sensing technology, BWTS will provide an innovative approach to enhance the sensing capability of underwater vehicles.**

***Index Terms*—Bionic whisker sensor, self-powered, triboelectric nanogenerator (TENG), wake perception.**

I. Introduction

FLOW field sensing technology is foundational for human exploration, development, and utilization of the oceans, playing a critical role in marine scientific research, resource exploration, ocean engineering, environmental monitoring, and underwater safety [1]. Conventional optical sensing techniques for underwater environments provide high-resolution recognition over short distances [2], [3]. Underwater acoustic sensing technology capitalizes on the ability of ultrasonic waves to travel long distances in water, making it widely used in applications such as underwater robot navigation, ship maintenance, and pipeline measurement [4], [5]. However, both optical and acoustic sensing technologies face significant challenges during underwater transmission, such as interference from ocean noise, multipath effects, and Doppler shifts [6]. For example, scattering of light caused by suspended particles in water results in reduced contrast and blurred edges of underwater objects [7]. Sound waves are susceptible to interference from ocean noise and obstacles, resulting in multipath effects and Doppler shifts [8]. Furthermore, as active sensing methods, both technologies encounter issues such as high energy consumption and structural complexity. As sensing technologies advance, it becomes increasingly clear that more versatile and adaptable sensing solutions are needed to meet the complex and evolving demands of underwater applications.

Marine mammals have developed highly sensitive perceptual systems [9], [10], [11], with seal whiskers being particularly effective in environmental sensing [12]. Researchers have leveraged these natural systems to develop a variety of sensors, including those based on piezoelectric effect [13], and capacitive effect [14], inspired by bionic seal whiskers. These sensors exhibit remarkable versatility, capable of detecting a wide range of stimuli such as static and dynamic touch, airflow, vibration, and even fluid flow [15], [16], [17]. This adaptability enhances the applicability of bionic whisker sensors in diverse fields, including environmental monitoring and scientific research [18], [19], particularly for underwater and surface applications. However, the complex fabrication processes required for these sensors often result in higher costs. Therefore, there is a need for more cost-effective, material-efficient, and easily fabricated designs to meet the growing demands of underwater sensing.

Triboelectric nanogenerator (TENG) is based on the synergistic effect of contact electrification and electrostatic induction [20], [21]. TENG can convert these stimuli into electrical signals and has already demonstrated exceptional performance in various fields, including human-computer interaction [22], human state sensing [23], renewable energy utilization [24], and monitoring sensing [25], [26]. Due to its flexible and adaptable structural design, along with its unique sensing mechanism, TENG exhibits high compatibility with aquatic environments. It plays a significant role in marine energy collection, environmental sensing, and underwater communication [27], [28]. Researchers have explored the potential of combining bionic concepts with TENG to design sensors for diverse applications. For instance, Wang et al. [29] developed a whisker sensor for underwater passive eddy current sensing, capable of detecting the different swinging states of a fish's tail. Varghese et al. [30] designed an artificial whisker sensor capable of detecting obstacles, while An et al.

Received 25 February 2025; revised 29 May 2025; accepted 30 May 2025. Date of publication 19 June 2025; date of current version 30 June 2025. This work was supported in part by the National Natural Science Foundation of China under Grant 52401399 and Grant 52371345 and in part by Xingliao Talent Plan Young Talent Project of Liaoning Province under Grant XLYC2203175. The Associate Editor coordinating the review process was Dr. George Dan Mois. *(Jianhua Liu, Siyuan Wang, and Yuanzheng Li contributed equally to this work.) (Corresponding authors: Siyuan Wang; Peng Xu; Minyi Xu.)*

The authors are with the State Key Laboratory of Maritime Technology and Safety, Marine Engineering College, Dalian Maritime University, Dalian 116026, China (e-mail: wsydlmu@dlmu.edu.cn; pengxu@dlmu.edu.cn; xuminyi@dlmu.edu.cn).

This article has supplementary downloadable material available at https://doi.org/10.1109/TIM.2025.3580836, provided by the authors.

Digital Object Identifier 10.1109/TIM.2025.3580836

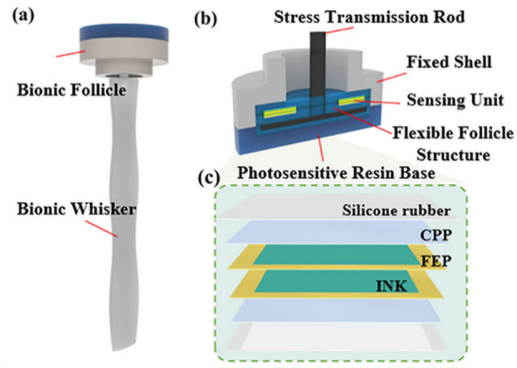

Fig. 1. Structural design. (a) Structure of BWTS. (b) Bionic follicle anatomy schematic. (c) Structure of sensing unit.

TABLE I
COMPARISON OF TRIBOELECTRIC WHISKER SENSORS

Ref.	Number of sensing units	Stationary object wake	Moving object wake
[29]	1	No	Yes
[30]	1	No	No
[31]	2	No	No
[32]	4	Yes	No
Our design	4	Yes	Yes

[31] developed a sensor that effectively identifies environmental features in the front and rear directions. However, the limited number of sensing units in these designs results in weak directional perception. Xu et al. [32] integrated four sensing units into the sensor to improve the directional perception capabilities. Nevertheless, this work can only measure the wake characteristics of stationary object, but does not achieve the wake perception effect of moving object. Therefore, it remains necessary to develop a sensor with robust directional perception to enable the detection of wakes generated by both stationary and moving underwater objects.

Inspired by seal whiskers, this article designs a bionic whisker triboelectric sensor (BWTS). It is mainly composed of bionic hair follicles and bionic whisker structures, as shown in Fig. 1(a). After the bionic whiskers sense the disturbance of the external flow field, they will drive the sensing unit inside the bionic follicles to generate electrical signals corresponding to the characteristics. Through simulation and experiments, it is proved that BWTS can sense the wake field characteristics generated by obstacle and underwater moving objects under various flow conditions. Its correlation with geometric parameters and motion parameters reaches 0.98–0.99. A detailed comparison of the excellent performance exhibited by the sensor proposed in this work can be found in Table I. The excellent underwater flow field perception ability will help underwater vehicles operate in complex environments.

II. DESIGN AND WORKING PRINCIPLE

A. Structural Design of BWTS

The BWTS proposed in this article mainly consists of bionic follicle and bionic whisker structures, as shown in Fig. 1(a).

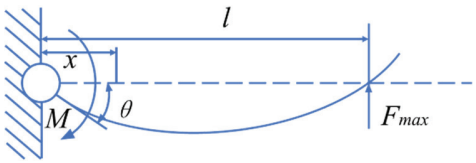

Fig. 2. Schematic of the force model.

The bionic follicle is designed as a flexible silicone structure embedded with four sensing units, with the flexible portion housed in a rigid shell to shield it from external environmental influences. Fig. 1(b) illustrates the detailed structure of the bionic follicle. The photosensitive resin base is connected to the fixed shell, which secures the cross-shaped flexible follicle structure made of silicone into the bionic follicle shell. The grooves in the fixed shell adopt a cross-shaped design, ensuring that the deformation of the flexible follicle under stress occurs in a fixed direction. This design enables the BWTS to exhibit directional output characteristics. The stress transmission rod and sensing units are enclosed within the flexible silicone follicle structure, with all four sensing units positioned at the center of the four arms of the cross-shaped structure. The detailed structure of the sensing units, shown in Fig. 1(c), consists of a fluorinated ethylene propylene (FEP) film printed with conductive ink, an interference-shielding cast polypropylene (CPP), and an externally wrapped silicone encapsulation layer. Conductive ink was printed on FEP film, which served as a dielectric layer. Two layers of FEP film, coated with conductive ink, were used to form the basic TENG, with a CPP electrostatic shielding film encapsulating the structure. The silicone rubber liquid and curing agent were mixed in equal proportions, poured into a mold, and allowed to cure. Subsequently, the four sensing units were placed into the grooves of the flexible substrate, encapsulated with silicone, and after curing, the stress transmission rod was inserted and encapsulated with silicone rubber again. Finally, the rigid whisker and stress transmission rod were assembled to the sensor preparation.

B. Working Principle of BWTS

When the BWTS is subjected to external stress, the end of the bionic tentacle will be displaced under the action of fluid-solid coupling. Combining the governing equations of the Euler-Bernoulli beam with fluid mechanics, a dynamic model of the BWTS under the stress of the wake field can be established. The vibration dynamic model of the bionic whisker can be modeled and analyzed using the Euler-Bernoulli undamped beam model with a uniform cross section, ignoring its axial strain and cross-sectional rotation, as shown in Fig. 2.

Considering only the maximum stress $F_{\max}$ of the wake field, the control equation of the Euler–Bernoulli undamped beam can be written as

$$EI\frac{\partial^4 w(x,t)}{\partial x^4}+c_s I\frac{\partial^5 w(x,t)}{\partial x^4 \partial t}+c_a\frac{\partial w(x,t)}{\partial t}+m\frac{\partial^2 w(x,t)}{\partial t^2}=-F_{\max}(l-x) \quad (1)$$

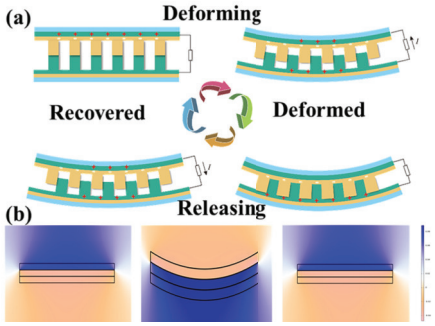

Fig. 3. Perception principle of BWTS. (a) Perceptual process. (b) Electrostatic simulation.

where c_s is the damping strain rate equivalent coefficient of the beam, c_a is the fluid damping coefficient, $w(x,t)$ is the displacement of the bionic whisker in the direction of flow velocity, m is the mass density of the whisker rod, E is Young's elastic modulus, and I is the second-order moment of the cross-sectional area of the bionic whisker.

Then, the bionic follicle is compressed inside to produce contact separation motion. Under open-circuit conditions, the output voltage of the sensing unit can be approximately expressed as

$$V_{\mathrm{OC}} = \frac{\sigma \cdot x(t)}{\varepsilon_0} \tag{2}$$

where ε_0 is the vacuum dielectric constant, σ represents the friction charge density per unit area, and $x(t)$ represents the distance between the two electrodes. The perceptual principle of BWTS is shown in Fig. 3(a). The bionic whisker will feel external stress $F_{\max}$ due to the change in the flow field. The stress transmission rod within the bionic follicle structure experience torque, applying compressive stress to the surface of the flexible follicle structure. This causes the sensing unit to bring the electrode layer into contact with the dielectric layer. During this interaction, free electrons on the surface of the electrode layer are transferred to the lowest molecular orbitals in the cross section of the dielectric layer, resulting from the overlap of electron clouds with different potentials. Once the vortex flow dissipates and moves away from the bionic whisker, the initial position inside the bionic follicle is restored. Free electrons flowthrough an external circuit to balance the local electric field. It can be seen from (2) that a change in $x(t)$ will drive a positively correlated change in the output voltage V_{oc}. Fig. 3(b) illustrates the potential distribution of the sensing unit over one contact separation cycle simulated using COMSOL software.

As shown in Fig. 4, the BWTS can improve the sensing capability of underwater robots. By obtaining the sensing characteristics of the BWTS, the relevant parameters of underwater objects can be known in real time.

III. Results and Discussion

A. Experimental Setup

In order to understand the relationship between the output electrical signal and displacement of the BWTS, an experiment plat was conducted using the LINMOT EI200-P01.

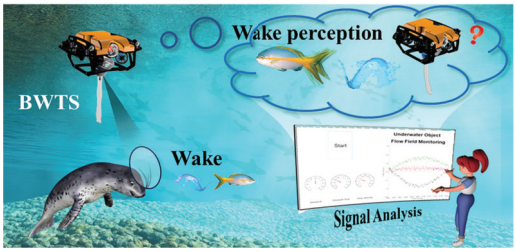

Fig. 4. Schematic of underwater sensing.

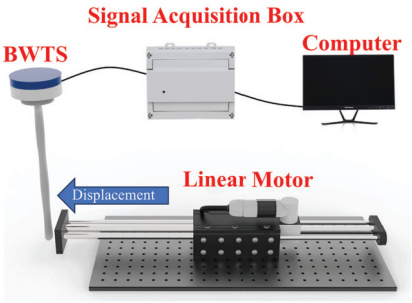

Fig. 5. Liner motor test platform of BWTS.

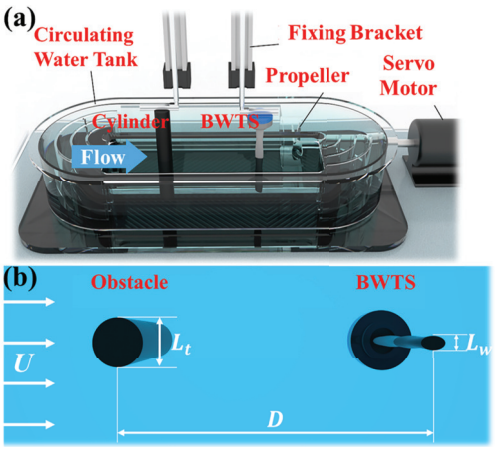

Fig. 6. Water tank test platform of BWTS. (a) Experiment platform. (b) Schematic of experimental parameters.

Different loads were simulated by adjusting the displacement and frequency parameters on the linear motor. The electrical signals were measured and collected using a multichannel signal acquisition box, as shown in Fig. 5.

To investigate the perceptual properties of the BWTS under the influence of changes in the obstacle wake field, we built a circulating flume experimental rig as shown in Fig. 6(a). The wake flow experiment was conducted in a $0.9 \times 0.25 \times 0.25$ m circulating water tank. The propeller was driven by a variable frequency servo motor to drive the fluid to flow through the guide plate in the water tank. The flow rate was achieved by adjusting the speed of the servo motor. The BWTS is fixed in the experimental section of the flume, and columns of different sizes are set in front to simulate the obstacle wake field. Sensing units 1 and 3 located at the two sides, and sensing units 2 and 4 located at the front and rear. Fig. 6(b)

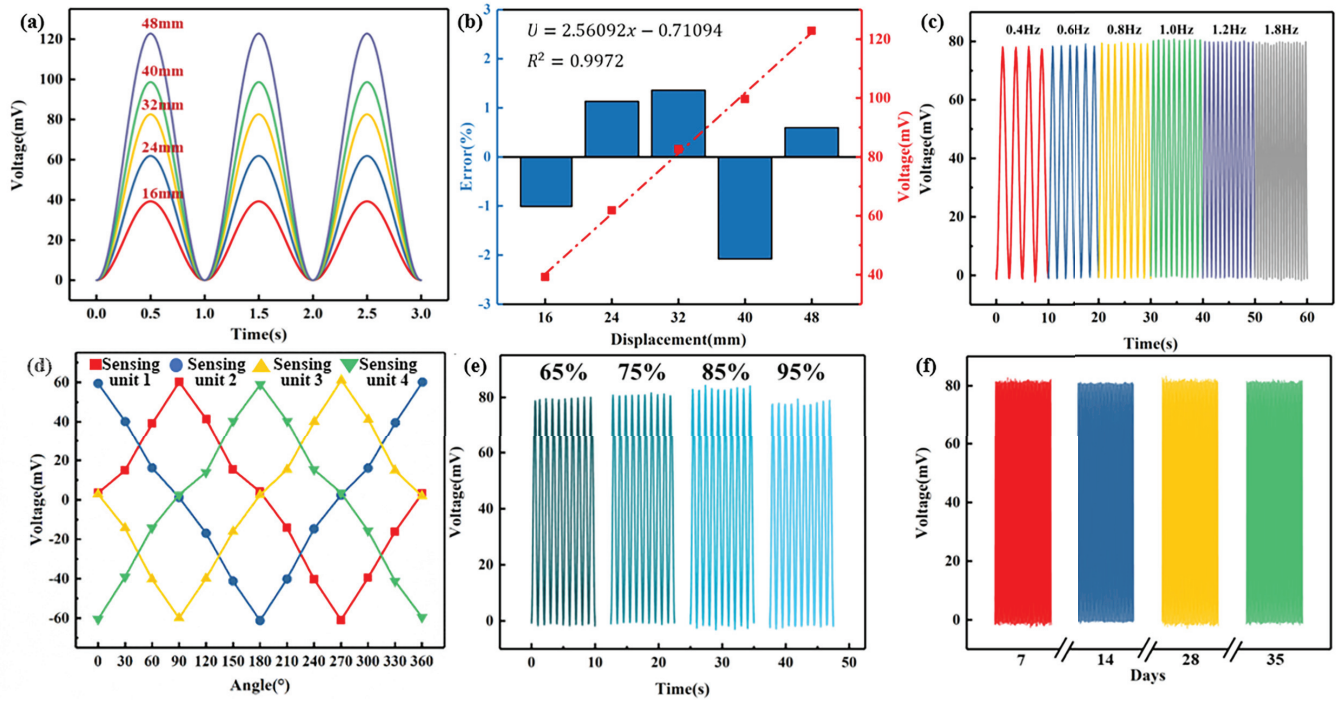

Fig. 7. Experimental results. (a) and (b) Correlation between whisker displacement and voltage of BWTS. (c) Voltage corresponding to the whisker displacement frequency from 0.4 to 1.8 Hz. (d) Output characteristics of the BWTS under different load directions. (e) Environmental adaptability. (f) Durability experiments.

demonstrates the parameter settings of the obstacle wake field sensing experiment.

B. Output Characterization of BWTS

The effect of whisker displacement on the output performance of the BWTS is shown in Fig. 7(a). The displacement ranges from 16 to 48 mm at a motion frequency of 1.0 Hz. As the displacement increases, the voltage of the sensing unit rises from 39.847 to 121.254 mV. The larger displacement facilitates more efficient charge transfer between the dielectric and electrode layers, leading to a gradual increase in voltage. Fig. 7(b) demonstrates the relationship between the voltage and the whisker displacement obtained using the leave-one-out cross-validation (LOOCV) method, which satisfies $U = 2.56092x - 0.71094$ and the correlation coefficient $R^2 = 0.9972$. This indicates that the relationship between the voltage and the whisker displacement approximates a linear function. Fig. 7(c) shows that the output voltage barely changes when the frequency increases from 0.4 to 1.8 Hz. From (1), it can be seen that the output voltage has no direct relationship with the frequency. The frequency of the output signal closely matches the displacement frequency, demonstrating that the BWTS has a high sensitivity to frequency changes. Fig. 7(d) shows how the output characteristics of the BWTS change with different load directions. The voltage changes of the sensing unit in different directions are caused by the different displacement components generated by the bionic whisker at various positions. These results indicate that the BWTS is highly sensitive to load direction, and the direction of force applied to the bionic whisker can be determined by comparing the signals from the four sensing units. Fig. 7(e) shows how the voltage of the BWTS changes with humidity, demonstrating that the voltage remains stable as humidity increases from 65% to 95%. This stability is attributed to the excellent sealing of the bionic follicle structure and the effective electrostatic shielding provided by the sensing unit. Fig. 7(f) presents the cycling results of the BWTS after 35 days of continuous operation under the same experimental conditions. The results show that the output signals remain stable even after more than a month, proving the BWTS's excellent durability.

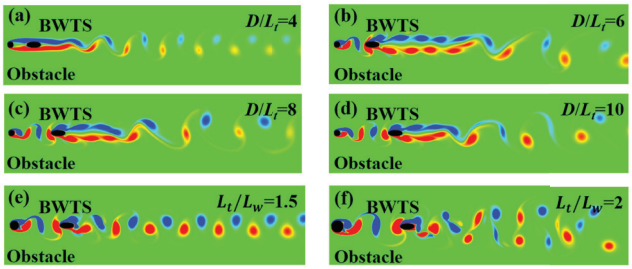

Fig. 8. Simulation results. (a) Flow field vorticity diagram in steady state when $D/L_t = 4$, (b) 6, (c) 8, and (d) 10. (e) Flow field vorticity diagram in steady state when $L_t/L_w = 1.5$ and (f) 2.

Obstacle and underwater moving object are common sensing objects in wake field sensing studies. Therefore, exploring the force characteristics of bionic whisker under the action of these two typical objects wake fields is crucial for an in-depth study of the sensing mechanism of BWTS. IBAMR software was used to numerically simulate the force characteristics of bionic whisker under the action of different obstacle wake fields in a rectangular channel with a computational domain

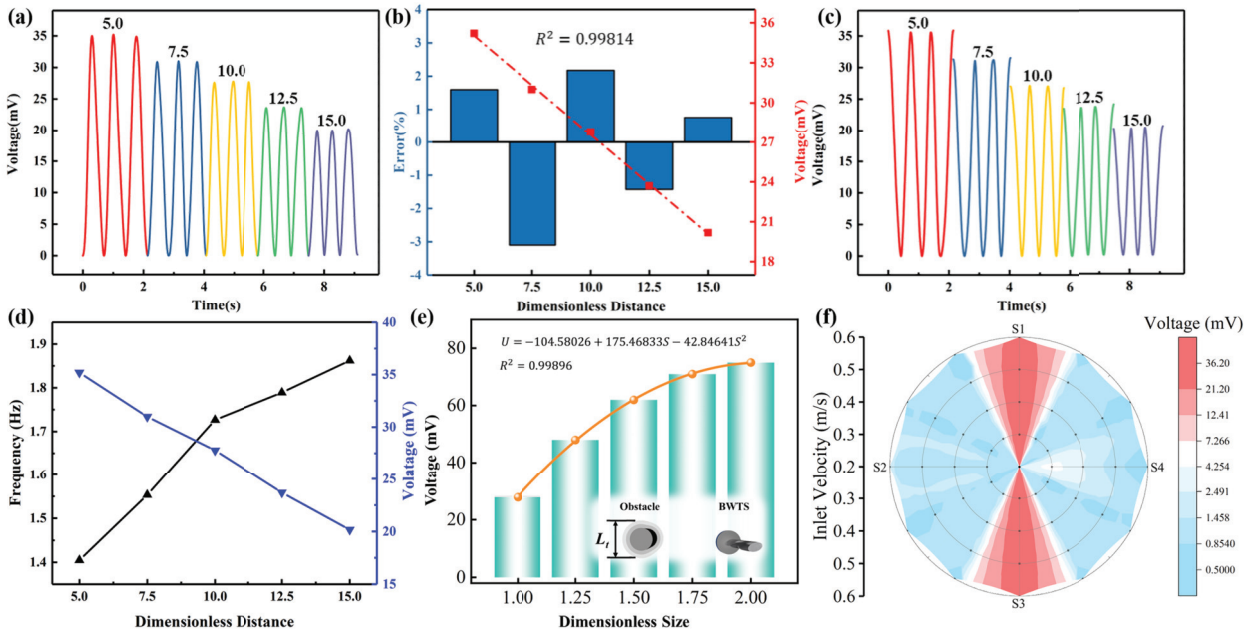

Fig. 9. Perception characteristics of BWTS to the wake field of obstacles. (a) and (b) Impact of the distance between obstacles and BWTS on the voltage of sensing unit 1. (c) Impact of the distance between obstacles and BWTS on the voltage of sensing unit 3. (d) Impact of the distance between obstacle and BWTS on the voltage and frequency of sensing unit 1. (e) Impact of the dimensionless size and (f) inlet flow velocity of obstacles on the voltage of sensing unit 1.

of $16D \times 32D$. The distance between the object and the whisker is expressed by the dimensionless parameter distance ratio D/L_t, the ratio between the circle center distance D and the object characteristic length L_t. Fig. 8(a) illustrates the state at $D/L_t = 4$. The shear layer from the obstacle occurs in the upstream side of the bionic whisker, where the shear layer reattachment phenomenon occurs. The 2-D cross section of the bionic whisker is elliptical, and this shape reduces the fluid resistance. The surface of the bionic whisker does not undergo obvious separation phenomenon. Fig. 8(b) demonstrates the vorticity map of the flow field at steady state at $D/L_t = 6$. It is evident that the shedding vortex street is formed simultaneously behind the obstacle and the bionic whisker. The bionic whisker is periodically affected by the vortex street behind it. During this process, the vortices formed by the two merges with each other, resulting in a "binary vortex street" behind the bionic whisker. Fig. 8(c) and (d) illustrates the vortex volume diagram of the flow field in the steady state at $D/L_t = 8$ and 10. Since the vortex is affected by the viscous resistance of the fluid and gradually dissipated during the movement, the force on the bionic whisker will gradually decrease. Thus, the maximum force position of the bionic whisker is at $D/L_t = 6$.

Next, we investigated the effect of obstacle size on the force characteristics of the bionic whisker. Based on the previous study, the optimal distance between the object and the bionic whisker is set to be constant as $D/L_t = 6$. Meanwhile, the dimensionless parameter size ratio L_t/L_w of the obstacle and the bionic whisker is used as a parameter to measure the size effect. L_t represents the characteristic length of the obstacle, and L_w represents the characteristic length of the bionic whisker. As shown in Fig. 8(e), when $L_t/L_w = 1.5$, the vortex street shed by the obstacle and the vortex street shed by the bionic whisker merge with each other better. The flow field behind the bionic whisker produces a periodically stable Karman vortex street, and the vortex scale is like the scale of the vortex street shed by the obstacle. Fig. 8(f) shows the situation when $L_t/L_w = 2.0$. The flow field state after the bionic whisker begins to show unstable vortex street structures at longer distances. Meanwhile, the intensity of vortex street shedding from the obstacle increases further. As the strength and position of the bionic whisker's shedding vortex street change, the vortex-induced vibration will become more obvious.

Subsequently, we investigated the effect of the distance between the BWTS and the obstacle on the output characteristics of the BWTS in a recirculating water tank. The vortex structures in the wake field are mainly distributed on both sides of the BWTS, and the signals outputted by the sensing units 1 and 3 contain the main characteristic information of the vortex structures. As shown in Fig. 9(a), the inlet flow velocity is set to be 0.302 m/s in this case, and the dimensionless size of the obstacle is 1.0. As the dimensionless distance increases from 5.0 to 15.0, the output voltage decreases from 35.052 to 20.123 mV. This result is due to the vortex structure in the wake field of the obstacle that dissipates gradually with the flow. The linear relationship between the voltage of the BWTS and the dimensionless distance can be expressed as $U = 42.51325 - 1.49471D$ with $R^2 = 0.99814$ as shown in Fig. 9(b), indicating that the sensing unit 1 good linear relationship between output voltage and dimensionless distance.

The output characteristics of sensing unit 3 are shown in Fig. 9(c), and due to the symmetry in the process of whisker displacement, there is a phase difference between the output signal of sensing unit 3 and that of sensing unit 1. When the output signal of sensing unit 1 reaches a peak, the output signal of sensing unit 3 reaches a minimum. The approximate position of the first vortex structure that flowed through the BWTS can be obtained by judging the sequence of the output signals of sensing units 1 and 3. Further, the amplitude and frequency of the output signals of sensing unit 1 are extracted by FFT transform, as shown in Fig. 9(d), which shows that the frequency of the output signals of sensing unit 1 increases with the increase of the dimensionless distance from 1.4 to 1.85 Hz gradually. Fig. 9(e) demonstrates the effect of obstacle size change on the output characteristics of sensing unit 1. The inlet flow velocity in this condition is 0.302 m/s, the dimensionless distance is set to 10.0, and the dimensionless size is subdivided from 1.00 to 2.00. As the size increases, the voltage of the BWTS gradually increases from 27.964 to 76.328 mV, and the relationship between the voltage of sensing unit 1 and the dimensionless size satisfies $U = -104.58026 + 175.46833S - 42.84641S^2$, and $R^2 = 0.99896$. The overall relative error is less than 8%, with good stability. Fig. 9(f) shows the effect of inlet flow rate on the voltage of the sensing unit under the condition of dimensionless distance of 10.0 and dimensionless size of 1.0. As the inlet flow rate increases, the voltage of sensing units 1 and 3 increases significantly. The output amplitude changes of sensing unit 4 is more obvious than that of sensing unit 2, but there is still a significant difference compared with the output of sensing units 1 and 3. The increase in flow rate causes the increase in vortex vibration of the whisker structure, which causes greater stress on the rear of the whisker structure.

For the force characteristics of the bionic whisker under the effect of underwater moving object wake field, we adopt a rigid airfoil to swing around the center to generate the wake field of the underwater moving object. The airfoil has an aspect ratio of 4:1, and the characteristic diameter is the same as the characteristic length of the whisker of the BWTS. Here, the dimensionless parameters are related

$$A_D = \frac{A}{L_f} \tag{3}$$

where A is the oscillation amplitude, L_f is the airfoil width, and A_D is the dimensionless oscillation amplitude. The distance between the underwater object and the bionic whisker is constant at $D/L_f = 6$, and the oscillation frequency f_t is constant at 1 Hz. As shown in Fig. 10(a), when $A_D = 2.0$, vortex structures with opposite directions appear alternately on the wake symmetry line. When $A_D = 4.0$, the shedding vortex in the proximity of the bionic whisker usually take the form of a pair of vortex structures with opposite rotations plus a separate vortex structure, as shown in Fig. 10(b). The increased strength of the shedding vortex structure generated by the underwater moving object under this condition leads to a significant increase in the bionic whisker force, but also leads to a more pronounced effect of the vortex-excited vibration caused by the bionic whisker's own shedding vortex structure.

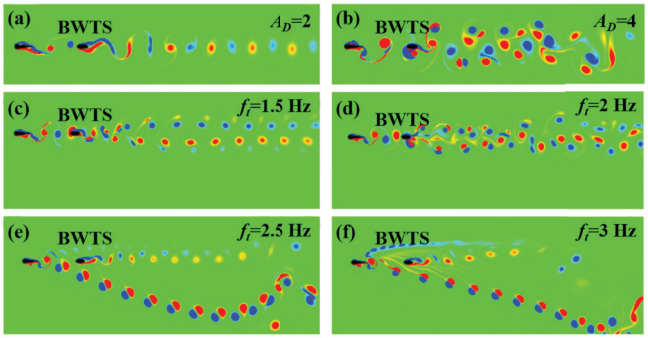

Fig. 10. Simulation results. (a) Flow field vorticity diagram in steady state when $A_D = 2$ and (b) 4. (c) Flow field vorticity diagram in steady state when $f_t = 1.5$, (d) 2, (e) 2.5, and (f) 3 Hz.

Subsequently, the law of the influence of the change of the oscillation frequency of the underwater object on the force on the bionic whisker was analyzed under the condition of $A_D = 2.0$. As shown in Fig. 10(c), at $f_t = 1.5$ Hz, vortex structures with opposite rotational directions are generated alternately, giving the bionic whisker an alternating stress effect. With the increase of the oscillation frequency to 2 Hz, the strength of the vortex structure in the wake field of the underwater object is enhanced, as shown in Fig. 10(d). When the oscillation frequency continues to increase to $f_t = 2.5$ Hz, the symmetry breaking phenomenon occurs in the wake flow field of the underwater object, as shown in Fig. 10(e). The vortex structure pairs generated by the underwater object pass farther from one side of the bionic whisker, and the pressure difference in the process causes the bionic whisker to be stressed. The influence of the underwater object's wake field on the formation of the bionic whisker's own wake field is reduced. As shown in Fig. 10(f), the symmetry breaking phenomenon caused by the underwater object oscillation at $f_t = 3.0$ Hz is more obvious, and the influence of the bionic whisker on the underwater object wake field is further reduced.

To further investigate the perception characteristics of the BWTS on the wake field of an underwater moving object, an airfoil structure is used to simulate the wake field of an underwater moving object, as shown in Fig. 11(a). The dimensionless distance is set to 10.0. As shown in Fig. 11(b), the dimensionless amplitude A_D of the voltage of the sensing unit 1 increases gradually from 2.0 to 6.0 at a swing frequency of 1.0 Hz. The increase of the pendulum amplitude of the underwater moving object leads to the enhancement of the strength of the vortex structure shed in the object wake flow field, which further causes the increase of the stress of the vortex structure on the whisker structure. Fig. 11(c) demonstrates the relationship between the voltage of the sensing unit 1 and the dimensionless swing amplitude, which satisfies $U = -40.81912 + 37.81354A_D - 2.92097A_D^2$, $R^2 = 0.98853$. Fig. 11(d) shows that the overall output trend of sensing units increases with the increase of swing amplitude, but the output of sensing unit 2 is significantly higher than that of sensing unit 4. When the flow passes through the whisker structure, the distribution of the anti-Karman vortex street generated by the swing relative to the wake symmetry line is far away from

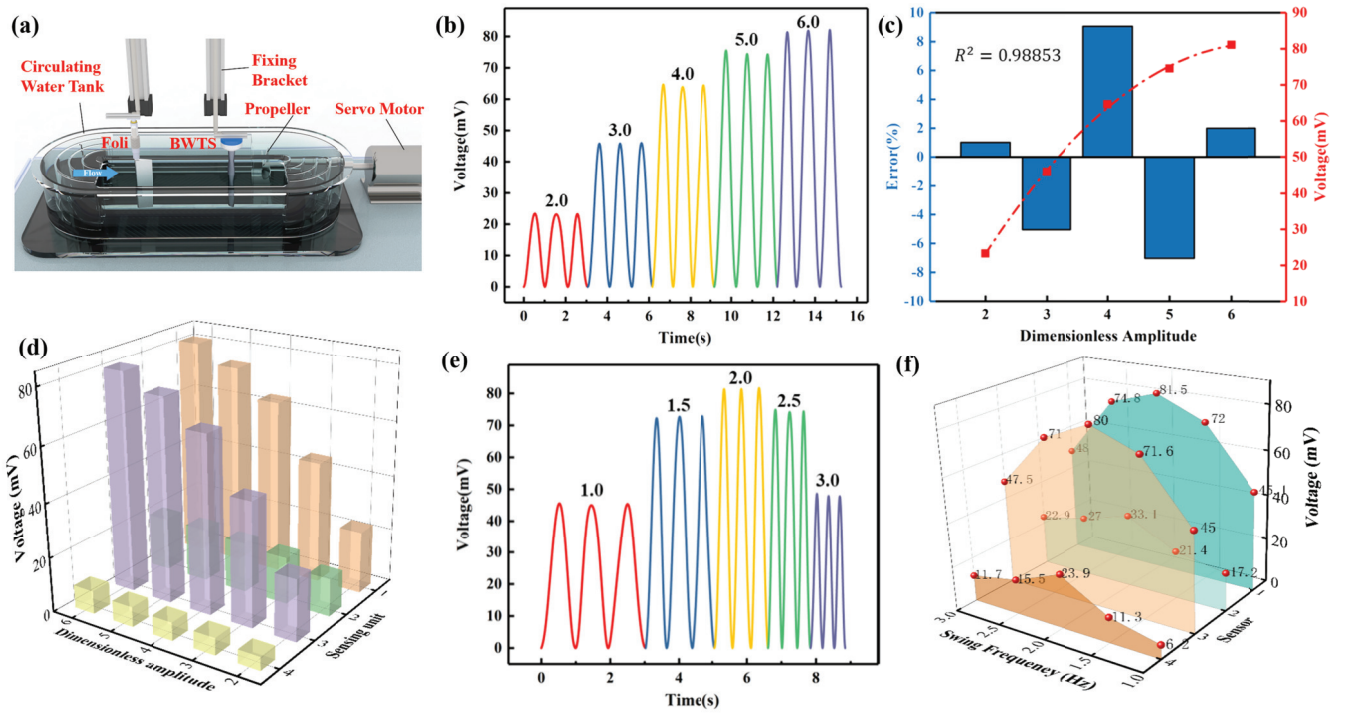

Fig. 11. Perception characteristics of BWTS to the wake field of an underwater moving object. (a) Experiment platform. (b) and (c) Impact of swing amplitude of on the voltage of sensing unit 1. (d) Relationship between voltage of all sensing units and swing amplitude. (e) Impact of swing frequency on the voltage of sensing unit 1. (f) Relationship between voltage of all sensing units and swing frequency.

the position of the vortex street structure. When the vortex structure flows through the whisker structure, the velocity component generated in the forward and backward directions is relatively larger. This further leads to a larger backward stress at the place where the swing amplitude is larger, thereby causing an increase in the output amplitude of the sensing unit 2. Then, the swing amplitude of the underwater moving object was controlled to be constant at A_D = 3.0, and the swing frequency of the underwater moving object was increased from 1.0 to 3.0 Hz to investigate the effect of the swing frequency of the underwater moving object on the output characteristics of the BWTS, as shown in Fig. 11(e). With the increase of the oscillation frequency, the output of the sensing unit 1 exhibits a trend of increasing and then decreasing, and the peak voltage reaches 81.854 mV. BWTS can achieve a more desirable voltage at the interval where the swing frequency lies around 2.0 Hz. As shown in Fig. 11(f), compared with the output feature information of the sensing units on both sides, the outputs of the front and rear sensing units 2 and 4 are relatively unstable due to the influence of the oscillation frequency of the underwater moving object, but the change trend of their output signals can still reflect the good perception ability of the oscillation frequency of the underwater moving object.

C. Application of BWTS in Real-Time Control

To test the real-time response capability of BWTS to external loads, an experimental device for driving light-emitting diodes using BWTS was designed, as shown in Fig. 12(a). The Arduino board was used for signal sampling and data processing. Fig. 12(b) shows the electrical schematic for controlling the light-emitting diodes. When the BWTS is displaced by external force, the Arduino controls the ON/OFF state of the light-emitting diodes through a threshold strategy. When the output voltage of one of the sensing units of the BWTS is within the preset signal interval, the designed control strategy identifies the displacement direction corresponding to the interval, and the Arduino outputs the corresponding switch value to light up the light-emitting diode. The accompanying figure in Fig. 12(c) shows the detailed configuration of the circuit used in the real-time control verification. When the BWTS is displaced in the direction of the sensing unit 4 under the action of external force, the connecting rod inside the BWTS is synchronously stressed with the sensing unit 2 and the sensing unit 4, and the contact separation occurs between the dielectric layers in the sensing unit 2 and the sensing unit 4, as shown in Fig. 12(c). Here, the microcontroller measures the change in the relative value of the output signal and lights up the corresponding light-emitting diode when it exceeds the set value. The demonstration is shown in Supplementary Video 1.

D. Application of BWTS in Wake Field Sensing

Subsequently, a visualization interface is constructed using MATLAB to further demonstrate the ability of BWTS to sense the wake field of underwater object. Combined with the relationship between the object parameters and the output signal fit above, the voltage of BWTS is converted into the corresponding parameters of the underwater object. The logic block diagram of underwater object characteristic information monitoring based on BWTS is shown in Fig. 12(d). After

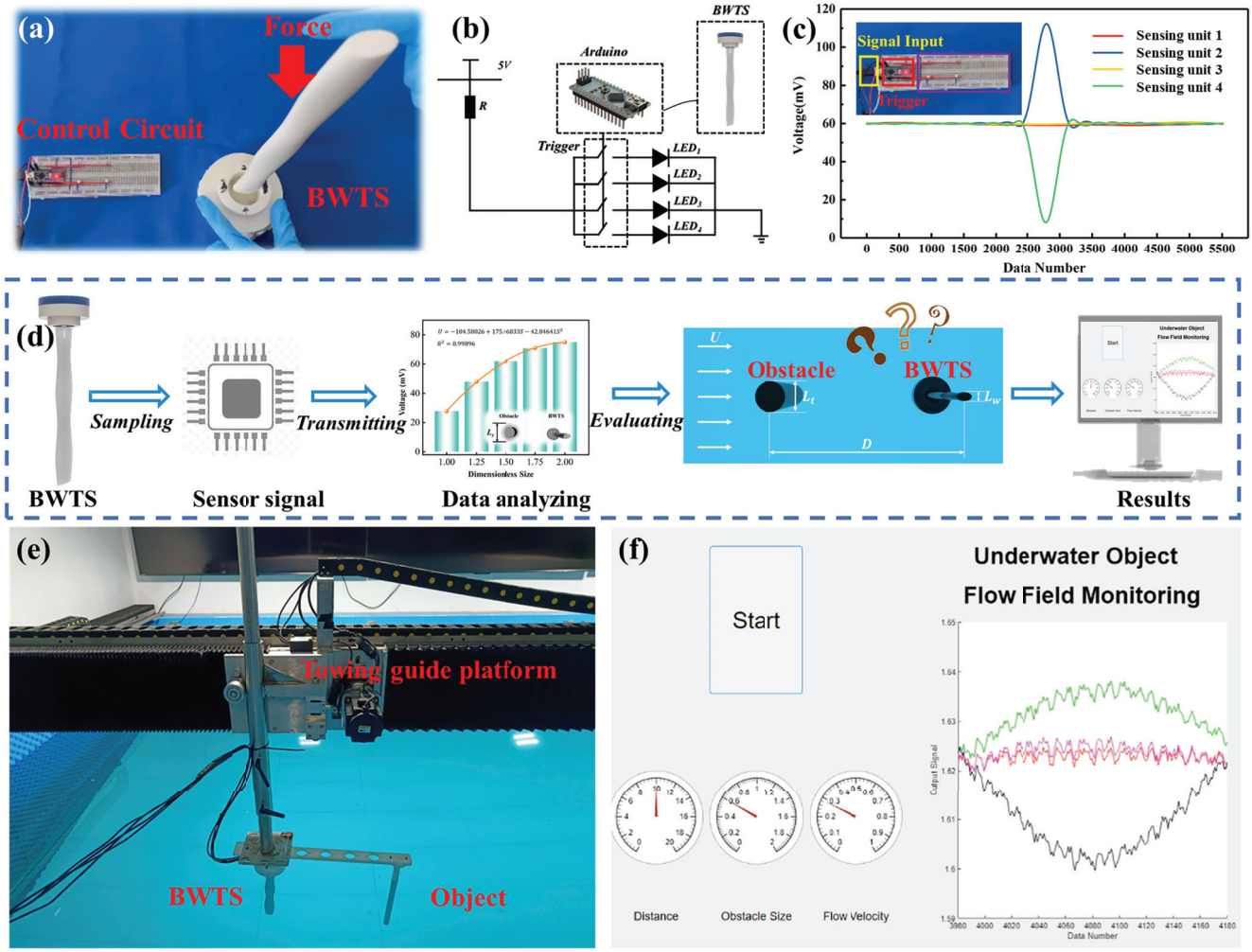

Fig. 12. Application of BWTS in real-time control and flow field sensing. (a) Real-time control experimental setup. (b) Experimental electronics for controlling LED lights. (c) Experimental data of real-time control based on BWTS. (d) Logic block diagram of underwater object characteristic information monitoring based on BWTS. (e) Experimental device. (f) Visualization interface.

the host computer collects the voltage of BWTS, it processes the data in real time and extracts the corresponding signal features in combination with the fit model, and then returns the processed underwater object characteristic information to the MATLAB visualization interface for display. The demonstration is conducted in a $6\times4\times1.5$ m pool, as shown in Fig. 12(e). The BWTS and the underwater object are fixed on the towing guide platform, and the underwater object situation is simulated by controlling the uniform motion of the towing guide platform in the x-direction. In this experiment, the distance between the obstacle and the BWTS is a known parameter. The towing guide platform runs at a speed of 0.3 m/s. Fig. 12(f) shows the specific data in the visualization interface during the experiment. When the towing guide platform starts to move, the output signal of BWTS is displayed on the interface. The predicted size and moving speed of the object are solved based on the above information, as shown in Supplementary Video 2. The error between the real-time feedback and the actual value is about 5.8%, which may be caused by the vibration of the guide rail.

IV. Conclusion

In this article, we combine the bionic whisker structure with a flexible sensing follicle based on TENG to construct a BWTS with a higher sensing dimension and stronger environmental adaptability wake perception capability. According to the structural design characteristics of BWTS, its output signal shows excellent linear relationship with the displacement of the whisker end. BWTS can obtain the wake field characteristics of obstacles and moving object under different parameter settings in the flow field environment by analyzing the change law of the characteristic signals of the four sensing units. The results obtained by numerical simulation analysis of the force characteristics of bionic whisker under the action of the wake flow field of different underwater objects using IBAMR software were verified. The correlation coefficient of BWTS for the geometric and motion parameters of underwater objects exceeds 0.98, and the error is less than 10%. BWTS can effectively identify the direction of load application by lighting up the LED in the corresponding direction. BWTS can also monitor various parameters of underwater objects

and provide real-time feedback on the monitoring panel. These prove that BWTS has a good perception ability of the wake field of underwater objects.

Currently, the perception range of a single sensor remains limited. In the future, we plan to conduct research on perception networks composed of multiple BWTS-based sensors to enable the detection of more comprehensive feature information. At the process level, stricter requirements will be imposed on the power consumption and size of the sensors to further enhance their perception accuracy. These performance improvements will play a critical role in ensuring the effective application of the sensors in actual working scenarios.

REFERENCES

[1] D. Q. Huy, N. Sadjoli, A. B. Azam, B. Elhadidi, Y. Cai, and G. Seet, "Object perception in underwater environments: A survey on sensors and sensing methodologies," *Ocean Eng.*, vol. 267, Jan. 2023, Art. no. 113202.

[2] J. S. Jaffe, "Underwater optical imaging: The past, the present, and the prospects," *IEEE J. Ocean. Eng.*, vol. 40, no. 3, pp. 683–700, Jul. 2015.

[3] Y. Wang et al., "Real-time underwater onboard vision sensing system for robotic gripping," *IEEE Trans. Instrum. Meas.*, vol. 70, pp. 1–11, 2021, doi: 10.1109/TIM.2020.3028400.

[4] Y. Bian, R. Li, G. Wang, X. Qin, M. Hu, and R. Ding, "Tightly coupled information fusion for SINS/DVL/USBL integrated navigation of UUV," *IEEE Trans. Instrum. Meas.*, vol. 72, pp. 1–13, 2023, doi: 10.1109/TIM.2023.3277945.

[5] H. Pan, K. Tang, J. Zhuo, Y. Lu, J. Chen, and Z. Lv, "Underwater acoustic technology-based monitoring of oil spill: A review," *J. Mar. Sci. Eng.*, vol. 11, no. 4, p. 870, Apr. 2023, doi: 10.3390/jmse11040870.

[6] K. M. Awan, P. A. Shah, K. Iqbal, S. Gillani, W. Ahmad, and Y. Nam, "Underwater wireless sensor networks: A review of recent issues and challenges," *Wireless Commun. Mobile Comput.*, vol. 2019, pp. 1–20, Jan. 2019, doi: 10.1155/2019/6470359.

[7] M. Jian, X. Liu, H. Luo, X. Lu, H. Yu, and J. Dong, "Underwater image processing and analysis: A review," *Signal Process., Image Commun.*, vol. 91, Feb. 2021, Art. no. 116088.

[8] J. Luo, Y. Han, and L. Fan, "Underwater acoustic target tracking: A review," *Sensors*, vol. 18, no. 1, p. 112, Jan. 2018.

[9] J. Liu et al., "Whisker-inspired and self-powered triboelectric sensor for underwater obstacle detection and collision avoidance," *Nano Energy*, vol. 101, Oct. 2022, Art. no. 107633, doi: 10.1016/j.nanoen.2022.107633.

[10] Y. Jiang et al., "Underwater source localization using an artificial lateral line system with pressure and flow velocity sensor fusion," *IEEE/ASME Trans. Mechatronics*, vol. 27, no. 1, pp. 245–255, Feb. 2022, doi: 10.1109/TMECH.2021.3062869.

[11] J. Wang et al., "Bioinspired whisker sensor based on orthometric FBGs for underwater applications," *IEEE Trans. Instrum. Meas.*, vol. 73, pp. 1–9, 2024.

[12] X. Zheng, A. M. Kamat, M. Cao, and A. G. P. Kottapalli, "Wavy whiskers in wakes: Explaining the trail-tracking capabilities of whisker arrays on seal muzzles," *Adv. Sci.*, vol. 10, no. 2, Jan. 2023, Art. no. 2203062, doi: 10.1002/advs.202203062.

[13] X. Zhang, X. Shan, T. Xie, J. Miao, H. Du, and R. Song, "Harbor seal whisker inspired self-powered piezoelectric sensor for detecting the underwater flow angle of attack and velocity," *Measurement*, vol. 172, Feb. 2021, Art. no. 108866, doi: 10.1016/j.measurement.2020.108866.

[14] W. C. Eberhardt et al., "Development of an artificial sensor for hydrodynamic detection inspired by a seal's whisker array," *Bioinspiration Biomimetics*, vol. 11, no. 5, Aug. 2016, Art. no. 056011, doi: 10.1088/1748-3190/11/5/056011.

[15] S. Fotouhi, S. Khayatzadeh, W. X. Pui, M. Damghani, M. Bodaghi, and M. Fotouhi, "Detection of barely visible impact damage in polymeric laminated composites using a biomimetic tactile whisker," *Polymers*, vol. 13, no. 20, p. 3587, Oct. 2021, doi: 10.3390/polym13203587.

[16] S. P. Wilson, P. F. M. J. Verschure, A. Mura, and T. J. Prescott, Eds., Biomimetic and Biohybrid Systems: 4th International Conference, Living Machines 2015, Barcelona, Spain, July 28–31, 2015, Proceedings, vol. 9222. Cham, Cham, Switzerland: Springer, 2015, doi: 10.1007/978-3-319-22979-9.

[17] J. T. Reeder, T. Kang, S. Rains, and W. Voit, "3D, reconfigurable, multimodal electronic whiskers via directed air assembly," *Adv. Mater.*, vol. 30, no. 11, Mar. 2018, Art. no. 1706733, doi: 10.1002/adma.201706733.

[18] Y. Yang et al., "Recent progress in biomimetic additive manufacturing technology: From materials to functional structures," *Adv. Mater.*, vol. 30, no. 36, Sep. 2018, Art. no. 1706539, doi: 10.1002/adma.201706539.

[19] P. Xu et al., "Deep-learning-assisted underwater 3D tactile tensegrity," *Research*, vol. 6, p. 62, Jan. 2023, doi: 10.34133/research.0062.

[20] V. G. Sirtoli, L. Morelli, R. J. Zednik, G. Cowan, and G. Gagnon, "Motion artifact modeling of capacitive electrodes based on triboelectric nanogenerators," *IEEE Trans. Instrum. Meas.*, vol. 73, pp. 1–10, 2024, doi: 10.1109/TIM.2024.3394480.

[21] Z. L. Wang, T. Jiang, and L. Xu, "Toward the blue energy dream by triboelectric nanogenerator networks," *Nano Energy*, vol. 39, pp. 9–23, Sep. 2017, doi: 10.1016/j.nanoen.2017.06.035.

[22] B. Shao et al., "Large-area, untethered, metamorphic, and omnidirectionally stretchable multiplexing self-powered triboelectric skins," *Nature Commun.*, vol. 15, no. 1, p. 1238, Feb. 2024.

[23] Y. Zou et al., "A bionic stretchable nanogenerator for underwater sensing and energy harvesting," *Nature Commun.*, vol. 10, no. 1, p. 2695, Jun. 2019, doi: 10.1038/s41467-019-10433-4.

[24] Y. Wang et al., "Flexible seaweed-like triboelectric nanogenerator as a wave energy harvester powering marine Internet of Things," *ACS Nano*, vol. 15, no. 10, pp. 15700–15709, Oct. 2021, doi: 10.1021/acsnano.1c05127.

[25] P. Xu et al., "A triboelectric-based artificial whisker for reactive obstacle avoidance and local mapping," *Research*, vol. 2021, Jan. 2021, Art. no. 9864967, doi: 10.34133/2021/9864967.

[26] J. Wen et al., "Design of a triboelectric nanogenerator-based sensor for velocity-displacement detection of high-speed switches," *IEEE Trans. Instrum. Meas.*, vol. 74, pp. 1–9, 2025, doi: 10.1109/TIM.2025.3529053.

[27] S. Wang et al., "Underwater triboelectric nanogenerator," *Nano Energy*, vol. 118, Dec. 2023, Art. no. 109018, doi: 10.1016/j.nanoen.2023.109018.

[28] J. Liu et al., "Underwater biomimetic lateral line sensor based on triboelectric nanogenerator for dynamic pressure monitoring and trajectory perception," *Small*, vol. 20, no. 19, May 2024, Art. no. 2308491, doi: 10.1002/smll.202308491.

[29] S. Wang et al., "Underwater bionic whisker sensor based on triboelectric nanogenerator for passive vortex perception," *Nano Energy*, vol. 97, Jun. 2022, Art. no. 107210, doi: 10.1016/j.nanoen.2022.107210.

[30] H. Varghese, V. Priya K, U. N. S. Hareesh, and A. Chandran, "Nanofibrous PAN-PDMS films-based high-performance triboelectric artificial whisker for self-powered obstacle detection," *Macromolecular Rapid Commun.*, vol. 45, no. 2, Jan. 2024, Art. no. 2300462, doi: 10.1002/marc.202300462.

[31] J. An et al., "Biomimetic hairy whiskers for robotic skin tactility," *Adv. Mater.*, vol. 33, no. 24, Jun. 2021, Art. no. e2101891.

[32] P. Xu et al., "Deep-learning-assisted triboelectric whisker for near field perception and online state estimation of underwater vehicle," *Nano Energy*, vol. 129, Oct. 2024, Art. no. 110011, doi: 10.1016/j.nanoen.2024.110011.

Jianhua Liu is currently pursuing the Ph.D. degree with Dalian Maritime University, Dalian, China.

His current research interests include underwater robot tactile system and underwater bionic nanogenerators.

Siyuan Wang is currently an Assistant Professor with Marine Engineering College, Dalian Maritime University, Dalian, China. His current research interests in self-powered sensing systems and applications, bionics, and underwater intelligent equipment.

Yuanzheng Li is currently pursuing the Ph.D. degree with Dalian Maritime University, Dalian, China.

His current research interests include the self-powered system, bionic sensors, and triboelectric nanogenerators.

Ziyue Xi is currently pursuing the Ph.D. degree with Dalian Maritime University, Dalian, China.

His current research interests include vibration energy, self-powered systems, and triboelectric nanogenerators.

Hao Jin is currently pursuing the Ph.D. degree with Dalian Maritime University, Dalian, China.

His current research interests include the underwater vehicle, bionic sensors, and underwater robotics.

Peng Xu received the Ph.D. degree with Dalian Maritime University, Dalian, China, in 2023.

His current research interests include self-powered sensing system and control, bioinspired design and control for marine and underwater robots, and triboelectric nanogenerators.

Minyi Xu received the Ph.D. degree from Peking University, Beijing, China, in 2012.

He is currently a Professor with the Marine Engineering College, Dalian Maritime University, Dalian, China. His current research interests include the areas of blue energy, self-powered systems, triboelectric nanogenerators, and its practical applications in smart ship and ocean.